nature portfolio

https://doi.org/10.1038/s41586-026-11072-8

Supplementary information

Lu^+ optical frequency references with accuracy verified at the 19th digit

In the format provided by the authors and unedited

Supplementary Information for Lu$^+$ optical frequency references with accuracy verified at the 19$^{\mathrm{th}}$ digit

K. J. Arnold,[1,2] M. D. K. Lee,[1] Qi Zhao,[1] Qin Qichen,[1] Zhao Zhang,[1] N. Jayjong,[1] and M. D. Barrett[1,3]

[1] *Centre for Quantum Technologies, National University of Singapore, 3 Science Drive 2, 117543 Singapore*
[2] *Temasek Laboratories, National University of Singapore, 5A Engineering Drive 1, 117411 Singapore*
[3] *Department of Physics, National University of Singapore, 2 Science Drive 3, 117551 Singapore*

TEMPERATURE ANALYSIS FOR BLACKBODY RADIATION SHIFT ASSESSMENT

The blackbody radiation (BBR) assessment is based on bounding the temperature between the ambient temperature within the enclosed space in which the chamber sits and the maximum temperature the ion could reasonably see. This consists of three main steps: evaluating the ambient environment temperature, evaluating the rf heating of the trap by measurements on an identical test trap, and assessing the maximum possible temperature rise of the trap electrodes by thermal modeling and simulation.

Lu-1 and Lu-2 sit inside a single enclosure on the same optical table. The ambient temperature inside the enclosure is continuously monitored by a thermistor that has been calibrated against a Pt100 sensor (Allectra 343-PT100-C2) with ±150 mK specified calibration uncertainty operating at 30 °C. The average temperature in the enclosure over the comparison measurement intervals was $T_\mathrm{e} = 300.15$ K with maximum deviation from the mean of ±150 mK (Fig. S1a) which is taken as the 1σ statistical uncertainty. Later measurements with multiple sensors calibrated against the same Pt100 sensor found a stable temperature gradient within the enclosure and the Lu-1 and Lu-2 vacuum chambers had temperature offsets of -53±220 mK and -246±220 mK relative to the central ambient temperature sensor and the 220 mK uncertainty accounts for the 440 mK temperature differential between top and bottom of the vacuum chamber. We estimate the ambient environment temperatures $T_\mathrm{e}^{(1)} = 300.10(31)$ K and $T_\mathrm{e}^{(2)} = 299.90(31)$ K where the uncertainty $\delta T_\mathrm{e}^{(k)}$ represents the combined statistical and sensor calibration uncertainties.

To determine the temperature increase of the ion trap due to rf heating, we performed in situ measurements on a third test trap of identical construction to Lu-1 and Lu-2. All traps have the construction shown in Fig. S1b. The rf power is delivered from a quarter-wave helical resonator through a single-pin vacuum feedthrough to two of the copper beryllium rod electrodes. The rf and dc electrode rods are held at both ends by ceramic spacers mounted in copper blocks. Iterations of this trap design have used either Macor (as for Lu-1) or Al_2O_3 (as for Lu-2) for the electrode spacers. The test trap was constructed twice with the two different ceramic materials using extra spacers from the original batches used in Lu-1 and Lu-2 construction. In both cases, the temperature

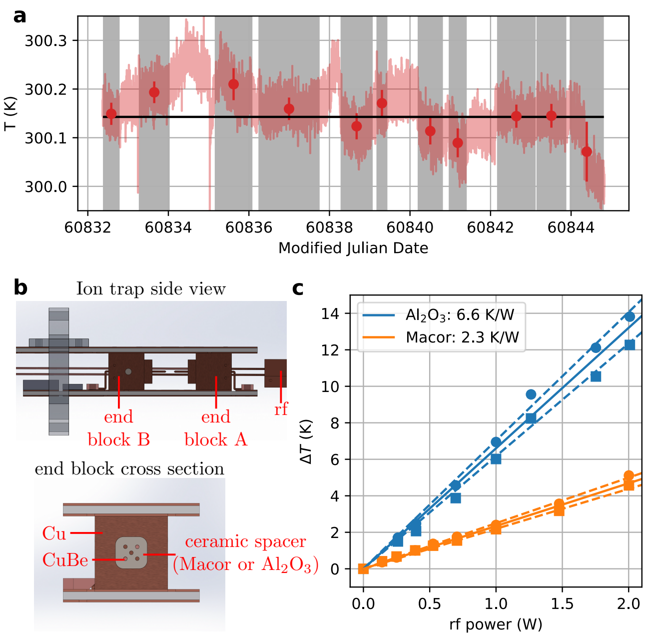

FIG. S1. **a,** Ambient air temperature measured in the clock table enclosure over the duration of the comparison campaign. Red points and error bars indicate the mean and standard deviation of temperature on the comparison measurement intervals. **b,** Ion trap construction. **c,** Measured temperature increase at end block A (squares) and B (circles) for the test trap with Al_2O_3 spacer (blue points) or Macor spacer (orange points).

at both end blocks was measured as a function of rf power in vacuum using Pt100 sensors, with the results shown in Fig. S1c. Both in-vacuum Pt100 sensors were calibrated against the same Pt100 reference sensor which was used to monitor the ambient environment. Taking the average of temperature readings from both ends, we observe a temperature increase of 6.6 K/W for the Al_2O_3 spacer and 2.3 K/W for the Macor spacer. In conjunction with the larger temperature rise, we note a significant difference in the loaded quality factor Q of the quarter-wave resonator, from an unloaded Q of 350 to a loaded Q of 240 (70) for the Macor (Al_2O_3) test traps, respectively. This is consistent with the difference in the loaded Q observed for Lu-1 and Lu-2, which are 190 and 50 respectively.

The implied dielectric loss tangent for the Al_2O_3 spacers was higher than expected and led us to further investigate with measurements on Al_2O_3 samples from an

	Power out (mW)				ΔT
Elec. at $\Delta T = 1$	P_s	P_rf	P_b	P_ec	
E_rf	-26.90	65.30	-16.74	-21.66	2.1
E_b	-26.90	-16.74	65.30	-21.66	1.5
E_ec	-1.77	-21.66	-21.66	45.09	2.2
Macor	25.76	62.48	16.03	20.73	

TABLE I. Power flow based on temperature differentials and heating from the Macor. For the first three rows, numbers give the power out of each electrode, with the indicated electrode being 1 degree above the others. The last row is the power flow into each electrode from the Macor. The total is taken to be half the total power into the resonator. We have taken $\kappa = 1.5\,\mathrm{Wm^{-1}K^{-1}}$ and the length of the Macor to be 5 mm. P_s denotes the power to the surrounding copper mount, the subscript rf denotes the rf electrodes, b the bias electrodes, and ec the end cap.

alternative supplier. However, these samples did not exhibit comparably high dielectric loss, even at relatively low specified purity (95%). It has been reported in the literature [1] that the loss tangent of Al_2O_3 varies widely between commercial suppliers, even at high purity ($> 99.5\%$), depending on the nature of the impurities. During the comparison measurements, both traps were operated with 0.25 W of rf power, implying a temperature increase of $\Delta T^{(1)}_\mathrm{eb} = 0.6\,\mathrm{K}$ and $\Delta T^{(2)}_\mathrm{eb} = 1.7\,\mathrm{K}$ at the copper end blocks of the respective traps.

The final consideration is the possibility of a temperature differential between the electrodes and the copper end blocks. The electrodes are bulk metal insofar as the skin-depth of rf currents is concerned and any reasonable estimate of currents from measured trap capacitance and resonator properties gives ohmic losses $< 1\,\mathrm{mW}$. A one-dimensional heat equation can be trivially solved to show that the electrode temperature is raised by no more than a small fraction of a degree above the temperature of the ceramic holders. Power is therefore assumed to be dissipated in the ceramic holders, which is intuitively obvious by the loading of the resonator. We take this power to be half the total rf drive power assuming equal dissipation at each end of the trap, i.e., all the power is dissipated in the ceramic. The most meaningful question concerns the temperature distribution across the ceramic. Specifically, is the maximum temperature likely to be higher than the overall measured temperature rise at the end blocks? A reasonable estimate can be made by solving the two-dimensional heat equation with a source term

$$q = \tfrac{1}{2}\sigma(\nabla V)^2$$

where V is the potential from the rf rods, σ is the effective conductivity accounting for the power loss, and the factor of 1/2 accounts for the time-averaged power dissipation. We can then calculate the total power absorbed by each electrode including the mounting block with σ adjusted to give the correct total power.

At equilibrium, the temperature rise of each electrode must be such that power into an electrode matches the power out. When an electrode is held ΔT above the others, Laplace's equation can be solved to determine the heat flow from that electrode into all other surfaces. We can then adjust ΔT for each electrode, including the outer block, to obtain a detailed balance of power in vs power out. In Table I we tabulate the power flows for a temperature differential of 1 degree for each electrode, and for the distribution of heat generation as indicated above. From symmetry, the two rf electrodes and the two bias electrodes behave identically so the power given is the total into or out of both for each pair. A self-consistent solution then requires ΔT given in the final column where we have taken $\kappa = 1.5\,\mathrm{Wm^{-1}K^{-1}}$ and the length of the Macor to be 5 mm. This would be the maximum temperature rise of the electrode above the measured mount temperatures. This neglects any other power loss in the system.

The solid angle subtended by the end cap electrodes is approximately 1.8% of the total solid angle, and that of the rf and bias electrodes is approximately 35%. Consequently, the maximum electrode temperature rise of $\Delta T^{(1)}_\mathrm{elec} = 2.2\,\mathrm{K}$ above the measured value for the end block temperature is likely conservative. For the trap using Al_2O_3 (Lu-2), the temperature rise $\Delta T^{(2)}_\mathrm{elec}$ is negligible due to the much higher thermal conductivity — by at least a factor of 10, and so the end block temperature is taken as the maximum.

Finally we estimate the minimum and maximum temperature bounds to be $[299.8, 303.2]\,\mathrm{K}$ for Lu-1 and $[299.6, 301.9]\,\mathrm{K}$ for Lu-2. The minimum temperature is taken to be $T^{(k)}_\mathrm{e} - \delta T^{(k)}_\mathrm{e}$. The maximum temperature is taken to be $T^{(k)}_\mathrm{e} + \delta T^{(k)}_\mathrm{e} + \Delta T^{(k)}_\mathrm{eb} + \Delta T^{(k)}_\mathrm{elec}$. For evaluating the BBR shift, we assume the temperatures $T_1 = 301.5(1.7)\,\mathrm{K}$ and $T_2 = 300.8(1.2)\,\mathrm{K}$ which are at the midpoints of the bounding intervals, with 1σ capturing the minima and maxima.

MAGNETIC FIELD SERVO DETAILS

For each chamber, a servo ensures that the magnetic field is disciplined to a setpoint B_set (Fig. S2a). Firstly, the field B is determined by measuring the linear Zeeman splitting of the ${}^3D_1\,|\,7,0\,\rangle$ to $|\,6,\pm1\,\rangle$ microwave transitions using Rabi spectroscopy, with a gain of $g = 1$, and a second-order integrator of $k = 0.1$. Secondly, the error $B_c = B_\mathrm{set} - B$ is servoed to zero by applying this correction field B_c at the ion by driving a shim coil.

As noted in [2], this second-order integrator eliminates servo error induced by a linear drift. An unnormalized discriminator, as opposed to a normalized one [3], is used to avoid servo errors: the usage of normalized discriminators in Rabi interrogation servos is known to lead to significant servo error due to time-correlations in flicker noise [4]. In addition, we note that the typical magnetic field correction applied to each ion over the duration of each experiment run is within about ± 50 nT, which only

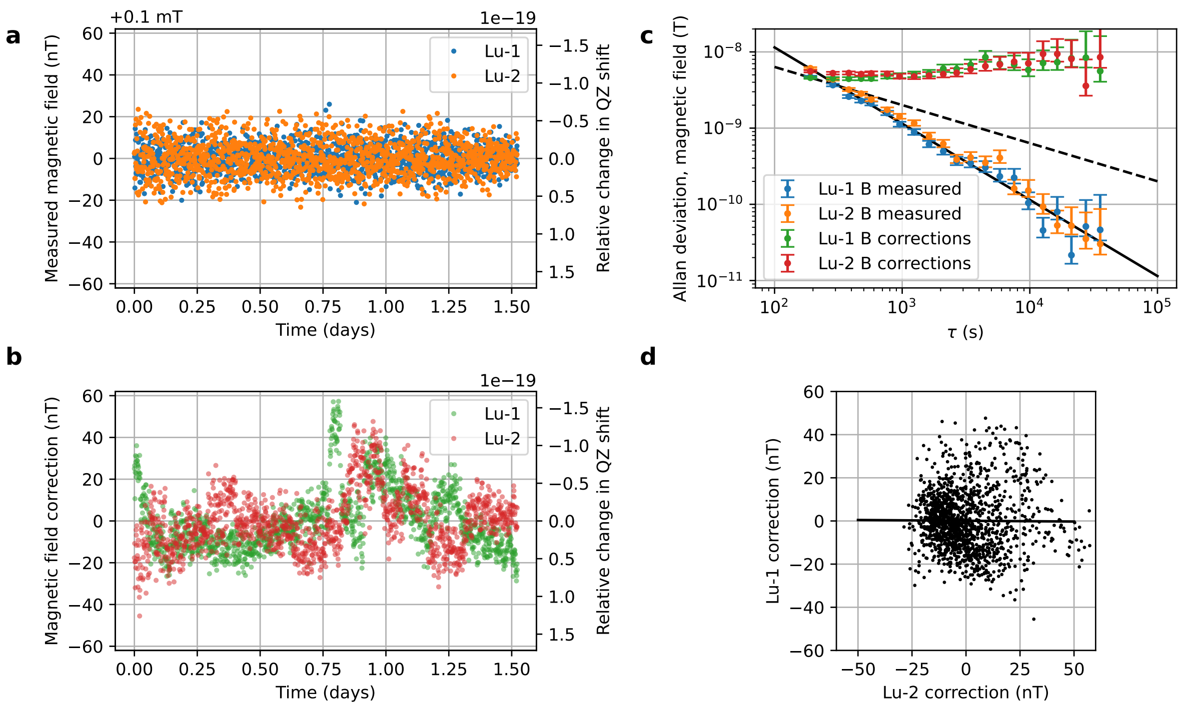

FIG. S2. **a,** Magnetic field disciplined to 0.1 mT at each ion. **b,** Applied field corrections for the longest experiment run, as an indication of the typical lab field stability. **c,** The Allan deviation of the measured magnetic field averages down as $1/\tau$ (solid black line), but the out-of-loop field measurement is used to assess the uncertainty in the field (dashed black line). **d,** Scatter plot of the data in **b** for which no significant correlation is observed. The black line is a linear fit and the Pearson correlation coefficient is $r = -0.009$.

corresponds to a relative change in the quadratic Zeeman shift at the $\sim 1\times10^{-19}$ level, per field interrogation (Fig. S2b). Any field servo error which scales with magnetic field flicker noise would lead to a significantly smaller shift (at least two orders of magnitude down, even with the more problematic normalized discriminator, according to simulations by [4]).

We observe that the measured magnetic field averages down as $1/\tau$ (Fig. S2c), but use the out-of-loop field measurement, which scales as $1/\sqrt{\tau}$, to assess the uncertainty in the field, because it is a representation of the field stability limited both by projection noise and the deadtime of the field measurements. The $1/\tau$ behavior of the measurements departs from $1/\sqrt{\tau}$ because by applying a correction on the field which is dependent on previous measurement points, the measurements are no longer independent. This behavior is consistent with simulations (Fig. S3) of servo operation which show that while the measured field may average as $1/\tau$, the actual compensated field averages as $1/\sqrt{\tau}$. Under zero-deadtime conditions, we expect the compensated magnetic field to have a stability following the projection noise limit. However, given that most of the time in each servo cycle is spent on the comparison, the duty cycle of the field measurement is only $\sim 1\%$, such that the field stability is above the projection noise limit and closer to the $2\times10^{-19}/\sqrt{\tau}$ stability estimated by the out-of-loop field measurement (Fig. S3a). In the hypothetical case of a 50% duty cycle, the field tracks closer to the projection noise limit (Fig. S3b).

The observed $1/\tau$ dependence of the measured field is an artifact of correlations between successive measurement points. Correlations between successive points are induced when projection noise is significant relative to the field noise. In the case of no field noise, an initial measurement B_i has its distribution centered at the actual field, $\tilde{B}_i = 0$, with a standard deviation of σ, the projection noise. Suppose the measured $B_i = \delta$. Consequently, the correction servo shifts the field, such that in the next servo iteration, $\tilde{B}_{i+1} = -\delta$, and B_{i+1} would now have its distribution centered about $-\delta$. As a result, there is a negative covariance between successive points: $C = \mathrm{cov}(B_i, B_{i+1}) < 0$. As shown in (1), the variance of the mean value would have both a $1/n$ and $1/n^2$ dependence, where n is the number of samples. Correspondingly, the Allan deviation of the measured field will have both a $1/\sqrt{\tau}$ and $1/\tau$ dependence.

$$\begin{aligned}
&\mathrm{var}\left(\frac{1}{n}\sum_{i=1}^{n} y_i\right)\\
&= \frac{1}{n^2}\left(\sum_{i=1}^{n}\mathrm{var}(y_i) + 2\sum_{i=1,i<j}^{n-1}\mathrm{cov}(y_i,y_j)\right)\\
&= \frac{1}{n^2}\left(n\sigma^2 + 2(n-1)C\right)\\
&= \frac{\sigma^2+2C}{n} - \frac{2C}{n^2}
\end{aligned} \tag{1}$$

We observe no correlations in the magnetic field corrections between the two ions (Fig. S2d), indicating that the magnetic field drifts at the two ions on slower timescales than the servo are uncorrelated. As noted in the manuscript, Ramsey coherence times on the microwave transitions in the individual traps relative to the contrast loss in correlation spectroscopy indicate that magnetic dephasing is also uncorrelated between the two systems.

COMPARISON DATA

Comparison data for all 11 runs is given in Table II.

Index	T_R s	C	τ h	y_{meas} 10^{-18}	u_{stat} 10^{-18}	y_{sys} 10^{-18}	u_{sys} 10^{-18}	y 10^{-18}
1	10.0	0.6	10.0	5.0	2.7	-0.24	0.10	5.26
2	5.0	0.9	18.4	-1.1	1.9	-0.29	0.10	-0.84
3	7.5	0.8	22.5	-0.8	1.6	-0.27	0.09	-0.53
4	5.0	0.9	36.5	0.2	1.3	-0.31	0.10	0.51
5	5.0	0.9	19.2	1.5	1.9	-0.31	0.10	1.76
6	5.0	0.9	6.6	0.8	3.2	-0.29	0.10	1.10
7	5.0	0.9	15.1	-1.5	2.3	-0.30	0.10	-1.24
8	5.0	0.9	10.8	-1.3	2.5	-0.30	0.10	-0.96
9	5.0	0.9	23.1	-0.9	1.7	-0.30	0.10	-0.60
10	5.0	0.9	17.9	-2.8	1.9	-0.31	0.10	-2.47
11	5.0	0.9	20.4	0.0	1.9	-0.30	0.10	0.30
Combined:			201	-0.30	0.57	-0.30	0.10	-0.01

TABLE II. Comparison measurement data from 11 runs. T_R is the Ramsey time used, C the contrast, τ the measurement duration in hours, y_{meas} the measured relative frequency difference, u_{stat} the projection noise limited uncertainty, y_{sys} the evaluated total systematic shift, u_{sys} the systematic uncertainty, and $y = y_{\mathrm{meas}} - y_{\mathrm{sys}}$ are the reported result for each measurement.

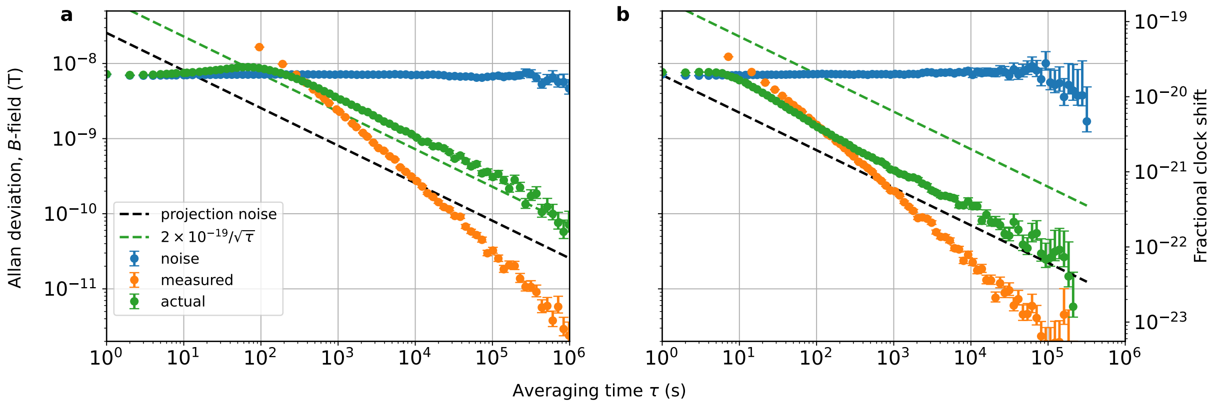

FIG. S3. Simulated magnetic field with flicker floor noise of 7 nT. **a,** Duty cycle as applicable to the comparison experiments. **b,** Duty cycle set to 50%. While the measured magnetic field has a $1/\tau$ dependence, the actual field stability has a $1/\sqrt{\tau}$ dependence which is limited both by projection noise and deadtime.

[1] R Vila, M Gonzalez, J Molla, and A Ibarra. Dielectric spectroscopy of alumina ceramics over a wide frequency range. *Journal of nuclear materials*, 253(1-3):141–148, 1998.

[2] Ekkehard Peik, Tobias Schneider, and Christian Tamm. Laser frequency stabilization to a single ion. *Journal of Physics B: Atomic, Molecular and Optical Physics*, 39(1):145–158, 2006.

[3] Pierre Dubé, Alan A Madej, Andrew Shiner, and Bin Jian. $^{88}Sr^{+}$ single-ion optical clock with a stability approaching the quantum projection noise limit. *Physical Review A*, 92(4):042119, 2015.

[4] Thomas Lindvall, AE Wallin, KJ Hanhijärvi, and Thomas Fordell. Noise-induced servo errors in optical clocks utilizing rabi interrogation. *Metrologia*, 60(4):045008, 2023.